# Modeling and Analysis of Sulfate Aerosols Processes in an Interactive Chemistry GCM.

S. Verma,[1] O. Boucher,[2] M. S. Reddy,[3] H. C. Upadhyaya,[1] P. Le Van,[4] F. S. Binkowski,[5] and O. P. Sharma,[1]

**Abstract.** An "online" aerosol dynamics and chemistry module is included in the Laboratoire de Météorologie Dynamique General Circulation Model (LMD GCM), so that the chemical species are advected at each dynamical timestep and evolve through chemical and physical processes that have been parameterized consistently with the meteorology. These processes include anthropogenic and biogenic emissions, over 50 gas/aqueous phase chemical reactions, transport due to advection, vertical diffusion and convection, dry deposition and wet scavenging. We have introduced a size-resolved representation of aerosols which undergo various processes such as coagulation, nucleation, dry and wet scavenging. The model considers 16 prognostic tracers: water vapor, liquid water, dimethyl sulfide (DMS), hydrogen sulfide ($H_2S$), dimethyl sulphoxide (DMSO), methanesulphonic acid (MSA), nitric acid ($HNO_3$), sulfur dioxide ($SO_2$), nitrogen oxides (NOx), carbon monoxide (CO), ozone ($O_3$), hydrogen peroxide ($H_2O_2$), sulfate mass and number for Aitken and accumulation modes. We provide a detailed description of the interactive chemistry module used in this study and evaluation of chemical species in winter and summer seasons. Aqueous phase reactions in cloud accounted for 71% of sulfate production rate, while only 45% of the sulfate burden in the troposphere is derived from in-cloud oxidation.

## 1. Introduction

The formation of sulfate aerosols in the atmosphere and its impact on climate is one of the challenging issues of scientific interest. Sulfate particles in the atmosphere alter the earth radiation budget directly and indirectly, by reflecting sunlight back to space and the interaction of particles with clouds [Twomey 1974; Kiehl and Briegleb 1993; Jones et al. 1994; Adams et al. 1999]. To address radiative impacts of sulfate aerosols atmospheric models must have explicit description of atmospheric chemistry (*i.e.* processes of aerosols formation, transport, and deposition). The inclusion of an interactive aerosol scheme in the general circulation models (GCMs) is one way to assess the aerosol impact on climate. There exist a limited number of global model studies that include size distributed aerosol modules [Ackermann et al. 1998; Wilson et al. 2001; Adams and Seinfeld 2002; Binkowski and Roselle 2003; Liao et al. 2003; Stier et al. 2004; Easter et al. 2004], still there exist areas of uncertainties especially arising from prescribed oxidant fields. Many of the global aerosol models predict mass concentration of aerosols, in contrast very few models which predict aerosol mass and number concentrations. The prediction of aerosol number concentration is very important step to reduce the uncertainty in the estimation of aerosol indirect radiative forcing. It also improves parametrization of clouds in the atmospheric models.

In this study a fully interactive sulfur chemistry module is developed and implemented in the Laboratoire de Météorologie Dynamique model General Circulation Model (LMD GCM) to simulate the number and mass distributions. It includes a detailed chemistry including gas- and aqueous-phase chemistry, and aerosol dynamics with recent evaluation for reaction mechanisms, rate constants that yield insight into the role of sulfate aerosols on climatic issues. All of the oxidant fields for sulfate formation to represent the aerosol evolution are calculated interactively. The size-segregated, two-moment distribution of sulfate aerosols, is predicted including processes like nucleation, condensation, coagulation, and interaction with clouds. The model predicted oxidants fields are compared with measurements and other estimates.

This paper presents a detailed description on how each process is simulated in this interactive module and presents the global budget of tropospheric sulfur compounds originating from natural and anthropogenic sources. The contribution of different processes to the sulfate aerosols is also presented.

## 2. Model Description

### 2.1. The atmospheric global model

This study uses the Laboratoire de Météorologie Dynamique model General Circulation Model. Detailed description of most of the model components have been presented in previous works [Boucher et al., 2002; Reddy and Boucher, 2004; Reddy et al., 2005a, 2005b; Hauglustaine et al., 2004]. Here we present a brief summary of the various model components. The model is a grid-point model

[1] Centre for Atmospheric Sciences, Indian Institute of Technology Delhi, New Delhi, India

[2] Laboratoire d'Optique Atmosphérique, CNRS / Université des Sciences et Technologies de Lille, 59655 Villeneuve d'Ascq Cedex, France

[3] NOAA-Geophyscial Fluid Dynamics Laboratory, Princeton, NJ

[4] Laboratoire de Météorologie Dynamique Ecole Normale Supérieure, 24 rue Lhomond, 75231 Paris Cedex 05, France

[5] Department of Environmental Science and Engineering, University of North Carolina, Chapel Hill, USA

with a resolution of 3.75° in longitude and 2.5° in latitude (corresponding roughly to the resolution of a T48 spectral model). It has 19 vertical layers in hybrid sigma-pressure coordinate, with 6 layers below about 600 hPa and 9 layers above about 250 hPa. The atmospheric transport is computed with a finite volume transport scheme for large-scale advection [van Leer, 1977; Hourdin and Armangaud, 1999], a scheme for turbulent mixing in the boundary layer, and a mass flux scheme for convection [Tiedtke, 1989]. The time step is thirty minutes for resolving the dynamical part of the primitive equations. Mass fluxes are cumulated over five time steps so that large-scale advection is applied every 15 minutes. The physical and chemical parameterizations are applied every 10 time steps (i.e., every 30 minutes). The different processes are handled through operator splitting.

### 2.1.1. Emissions

Our sulfur scheme considers DMS, $SO_2$, $H_2S$, DMSO, MSA, and sulfate. The sulfur emissions from fossil fuel combustion and industrial processes are from GEIA (Global Emission Inventory Activity) (Table 1). A fixed percentage of 5% sulfur from combustion sources is assumed to be directly emitted as sulfate. There is a small additional source of sulfur under of the form of anthropogenic $H_2S$. The global total of anthropogenic sources is 64.9 Tg S yr$^{-1}$ and represents year 1984. We also consider DMS biogenic emissions from marine biosphere; flux of which is derived from sea surface DMS concentrations of Kettle et al. [1999] and the sea to air parametrization of Liss and Merlivat [1986]. The global marine DMS emissions are equivalent to 20.7 Tg S yr$^{-1}$. In addition, there is relatively small contribution from the continents, where vegetation and soils emit both DMS and $H_2S$. Emission of $H_2S$ and DMS from the biosphere and emission of $SO_2$ from biomass burning are same as described in Boucher et al. [2002].
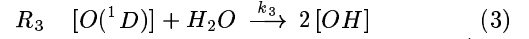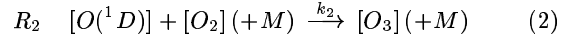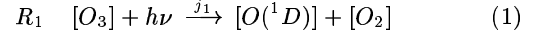
### 2.2. Chemistry and aerosol modules

The chemical transport model propagates the model state forward in time from the initial state to the final state. The atmospheric concentrations all sulfur species (DMS, $H_2S$, DMSO, MSA, $SO_2$, sulfate) and oxidants (OH, $O_3$, $H_2O_2$) are set to zero as initial values. Other chemical species which influence the atmospheric oxidant concentrations are initialized with their typical atmospheric concentrations: CO with 96 ppbv, NOx and $O_3$ with 1 ppbv, $NH_3$ with 0.5 ppbv over ocean, 1.5 ppbv over land, and 0.2 over ice. All of the important gaseous and aqueous phase reactions are considered to calculate oxidants and sulfate aerosols.

### 2.2.1. Gas-phase chemistry

The gas phase reactions and reaction rates are those described by Chen and Crutzen [1994] and Lawrence et al. [1999]. Although there are many species that contribute to sulfate formation through gas phase reactions in the atmosphere, for simplicity of tropospheric chemistry in this model, we consider a system of chemical reactions involving $SO_2$, $O_3$, $CH_4$, CO, $NO_X$, and DMS. The hydroxyl radical, produced through various photochemical reactions in the atmosphere, plays an important role in gas-phase chemistry by acting as powerful oxidizing medium in many reactions. Hydroxyl radicals react with nearly every molecular species in the atmosphere [Berge, 1993; Atkinson et al., 1989].

In the gaseous phase sulfur dioxide is oxidized to sulfate by a series of chain reactions initiated by OH. The parametrization of DMS oxidation has been constructed assuming that DMS reacts with OH and $NO_3$. DMS is oxidized by $NO_3$ and OH radical producing $SO_2$ and DMSO, which is further oxidized to produce $SO_2$ and MSA. The reactions and reaction rates for DMS are following from Atkinson et al. [1989] and Chatfield and Crutzen [1990].

The present model considers a fully explicit mechanism for 33 chemical/photochemical reactions in gas-phase. The reactions and their corresponding rates are tabulated in Table 2. The reaction rates are updated at each model time step based on the ambient conditions (temperature, pressure, etc.) in each grid box. A quasi-steady state approximation (QSSA) is applied to obtain the concentration of various species. For example, reactions ($R_1 - R_3$), in Table 2, can be represented as:

$$R_1 \quad [O_3] + h\nu \xrightarrow{j_1} [O(^1D)] + [O_2] \tag{1}$$

$$R_2 \quad [O(^1D)] + [O_2](+M) \xrightarrow{k_2} [O_3](+M) \tag{2}$$

$$R_3 \quad [O(^1D)] + H_2O \xrightarrow{k_3} 2[OH] \tag{3}$$

If $j_1$, $k_2$ and $k_3$ denote the rates of $R_1$, $R_2$ and $[O(^1D)]$ quenching, respectively, then the rate of formation for $[O(^1D)]$ is given by,

$$\frac{d[O(^1D)]}{dt} = j_1[O_3] - k_2[O(^1D)][O_2] - k_3[O(^1D)][H_2O]$$

Applying the steady-state approximation to the above equation, i.e. by setting the tendency of $[O(^1D)]$ to zero, we obtain,

$$[O(^1D)] = \frac{j_1[O_3]}{k_3[H_2O] + k_2[O_2]} \tag{4}$$

Similarly from reaction $R_{11}$, $R_{12}$ and $R_{13}$ in Table 2, we get,

$$[H_2O_2] = \frac{k_{11}[HO_2]^2}{j_{12} + k_{13}[OH]} \tag{5}$$

The net rate of formation to determine the [OH] and [$HO_2$] radicals from precursor concentration are,

$$\frac{d[OH]}{dt} = [P_1] - [L_1][OH] \tag{6}$$

$$\frac{d[HO_2]}{dt} = [P_2] - [L_2][HO_2] - 2k_{11}[HO_2]^2 \tag{7}$$

The concentration of [$HO_x$] can thus be obtained by applying QSSA to Eqns. (6) and (7) giving

$$[P_1] - [L_1][OH] = 0 \quad or \quad [OH] = \frac{[P_1]}{[L_1]} \tag{8}$$

$$[P_2] - [L_2][HO_2] - 2k_{11}[HO_2]^2 = 0 \tag{9}$$

where terms $[P_1]$, $[L_1]$, $[P_2]$ and $[L_2]$ denote,

$$[P_1] = 2k_3[O(^1D)][H_2O] + 2j_{12}[H_2O_2] + k_9[NO][HO_2] + k_{10}[O_3][HO_2] + j_{26}[HNO_3]$$

$$[L_1] = k_4[CH_4] + k_8[CO] + k_{13}[H_2O_2] + k_{14}[SO_2] + k_{15}[NO_2][M] + k_{27}[O_3] + k_{28}[HO_2] + [term1]$$

$$[term1] = [k_{29} + k_{32}][DMS] + k_{30}[H_2S] + k_{31}[DMSO] + k_{19}[HNO_3]$$

$$[P_2] = k_6[O_2][CH_3O] + 2\beta j_{7b}[CH_2O] + k_8[CO][OH] + k_{13}[OH][H_2O_2] + k_{14}[OH][SO_2] + k_{27}[OH][O_3] + k_{30}[H_2S][OH]$$

$$[L_2] = k_9[NO] + k_{10}[O_3] + k_{28}[OH]$$

Further simplification of (9) is achieved by substituting the steady state concentrations of $[CH_3O]$, $[CH_2O]$ and $[H_2O_2]$, which leads to the following quadratic equation for $[HO_2]$,

$$a_0[HO_2]^2 + b_0[HO_2] - c_0 = 0 \qquad (10)$$

where $a_0$, $b_0$, $c_0$ and other terms are expressed as,

$$a_0 = 2k_{11}$$
$$b_0 = k_{28}[OH] + c_1(1 - d_0)$$
$$c_0 = \left(2k_3[O(^1D)][H_2O] + 2j_{12}[H_2O_2] + j_{26}[HNO_3]\right)d_0$$
$$+ \left(\frac{4\beta j_{7b}bk_{33}}{\alpha j_{7a} + \beta j_{7b}}\right)[DMS][NO_3]$$
$$d_0 = \left(\frac{c_2 + k_{13}[H_2O_2]}{c_3}\right)$$

$$c_1 = k_9[NO] + k_{10}[O_3]$$
$$c_2 = \left(1 + \frac{2\beta j_{7b}}{\alpha j_{7a} + \beta j_{7b}}\right)k_4[CH_4] + k_8[CO] + k_{14}[SO_2] +$$
$$\left(\frac{2\beta j_{7b}}{\alpha j_{7a} + \beta j_{7b}}\right)[term2] + k_{30}[H_2S] + k_{27}[O_3]$$

$$[term2] = 2k_{29}[DMS] + [1.5k_{32} + 1.2k_{33}][DMSO]$$

$$c_3 = k_4[CH_4] + k_8[CO] + k_{13}[H_2O_2] + k_{14}[SO_2] +$$
$$k_{15}[NO_2][M] + k_{27}[O_3] + k_{28}[HO_2] + [term2]$$

Now, the steady-state concentrations of $[H_2O_2]$, $[OH]$ and $[HO_2]$ are obtained from Eqns. (5), (8) and (10) iteratively. The iterative process is continued till the convergence is achieved (generally 3 to 4 iterations are required for the process to converge).

At nighttime the gas-phase chemistry is considerably simplified because of the absence of sunlight and thus of the associated photochemical reactions. Therefore, concentrations of OH are set to zero at night time. Once the concentrations of the short-lived radicals (OH and HO$_2$) have been computed, the photochemical production and loss terms of the transported species are calculated numerically [Hesstvedt et al., 1978] using

$$C(t + \Delta t) = \frac{P}{L} + \left[C(t) - \frac{P}{L}\right]\exp\{-L\,\Delta t\} \qquad (11)$$

$C(t)$ denotes the concentration of species at time $t$; $P$ and $L$ denote production rate (mol cm$^{-3}$ s$^{-1}$) and loss rate (s$^{-1}$) of that chemical species, respectively. For example the rate expressions for estimating DMS and SO$_2$ can be derived from Table 2 reactions as;

$$\frac{d[DMS]}{dt} = -[k_d[OH] + k_{33}[NO_3]]\quad[DMS]$$
$$k_d = k_{29} + k_{32}$$
$$\frac{d[SO_2]}{dt} = [P_3] - k_{14}[OH][SO_2]; \quad [SO_2]_{st} = \frac{[P_3]}{k_{14}[OH]}$$
$$\frac{d[H_2SO_4]}{dt} = k_{14}[OH][SO_2]$$

$$[P_3] = k_d[DMS][OH] + k_{30}[H_2S][OH]$$
$$+ k_{31}[DMSO][OH] + k_{33}[NO_3][DMS]$$

the next time step values of [DMS], [SO$_2$] and [H$_2$SO$_4$] are updated using

$$[DMS]_{t+\Delta t} = [DMS]_t \exp\{-k_d[OH]\Delta t\} \qquad (12)$$

$$[SO_2]_{t+\Delta t} = [SO_2]_{st} + ([SO_2]_t - [SO_2]_{st})\exp\{-k_{14}[OH]\Delta t\} \qquad (13)$$

$$[H_2SO_4]_{t+\Delta t} = [H_2SO_4]_t + k_{14}[SO_2][OH]\Delta t \qquad (14)$$

The chemical transformations in the model are therefore handled efficiently with the semi-analytical numerical method of Hesstvedt et al. [1978], though there is a slight loss of accuracy compared to more elaborate schemes (e.g., a fast Gear solver). The intention of this scheme is to maintain the correct qualitative relationship between the concentration of each precursor species and its rate of production and loss. This scheme is applicable due to longer lifetimes of all the prognostic chemical species considered here and it makes it easier to compute a mass-balanced sulfur budget. The photolytic rates are significantly modified in the presence of clouds, the gas-phase chemistry module also takes into account the cloud effects. In the model, clear sky photolysis rates are multiplied by a correction factor to account for these effects,

$$j = j_{clear}[1 + a(F_{cld} - 1)] \qquad (15)$$

where $j$ is the photolysis rate in the grid containing clouds, $a$ is the fractional area of cloud coverage, and $F_{cld}$ is the ratio of the cloudy sky to clear sky photolysis rate coefficient, which depends on the location in the grid column [Chang et al., 1987].

### 2.2.2. Aqueous-phase chemistry

In-cloud aqueous-phase reactions are major contributors to atmospheric sulfate. In the present model aqueous-phase oxidation by O$_3$ and H$_2$O$_2$ are considered. The SO$_2$, H$_2$O$_2$ and O$_3$ concentration in cloud droplet precipitation are assumed to be in equilibrium with the gas-phase concentration and are carried as implicit fields i.e. they are computed as a function of gas-phase concentrations. CO$_2$ concentration is held constant (360 ppm) throughout the model integration. The aqueous-phase mechanism is active only in the cloudy portion of the grid box and in the presence of liquid water. The aqueous phase oxidation in ice clouds is not considered here. In the parameterization of aqueous phase chemistry, the starting step is the Henry's law

$$[M] = K_H P_M\,(mol\,l^{-1}) \qquad (16)$$

where $P_M$ is the partial pressure of species M. For gases that undergo rapid reversible aqueous-phase reactions such as acid-base ionization equilibria, an effective Henry's law coefficient, $K_H^*$ can be defined [Schwartz, 1986]. As an example, the $K_{SO_2}^*$ (effective Henry's law coefficient for SO$_2$), considering aqueous-phase reactions R$_5$, R$_6$ and R$_7$ from Table 3 can be defined as

$$[S(IV)] = K_{SO_2}^* P_{SO_2} \qquad (17)$$

$[S(IV)] = ([SO_2.H_2O] + [HSO_3^-] + [SO_3^-])$ refers to the total concentration of dissolved SO$_2$ species in the cloud water

$$K_{SO_2}^* = \left[1 + \frac{K_6}{[H^+]} + \frac{K_6 K_7}{[H^+]^2}\right]H_5 \qquad (18)$$

where $K_6$ and $K_7$ are first and second ionization constants for sulfurous acid; $H_5$ is the dissociation constant for SO$_2$ (Table 3). $P_{SO_2}$ is the partial pressure of SO$_2$ in gas-phase

(atm).

The equations for chemical equilibrium of $SO_2$-$NH_3$-$CO_2$-$HNO_3$-$H_2O$ system have been taken from Chen and Crutzen [1994]. The units for Henry's constant (K) and dissociation constant (H) are in M and M atm$^{-1}$, respectively, and are summarized in Table 3. The model represents a simplified version of the aqueous model of Walcek and Taylor [1986] and it is similar to an earlier equilibrium model of Ohta et al. [1981]. In our description of the process we assume that aqueous equilibrium and electro neutrality are continuously maintained [Pandis and Seinfield, 1989; Ohta et al., 1981] so that the equilibrium hydrogen ion concentration in clouds may be obtained by considering the following electro neutrality equation,

$$
\begin{aligned}
[H^+] + [NH_4^+] \ = \ & [OH^-] + [HCO_3^-] \\
& + 2[CO_3^{2-}] + [HSO_3^-] + 2[SO_3^{2-}] \\
& + [HSO_4^-] + 2[SO_4^{2-}] + [NO_3^-]
\end{aligned} \quad (19)
$$

From the initial partial pressure ($P_i^\circ$) of gas $i$ under equilibrium conditions in the clouds, the final pressure $P_i$ can be expressed as:

$$
P_{NH_3} = \frac{\frac{P_{NH_3}^\circ}{RT} \frac{10^6}{W}}{\frac{K_{14}H_{13}[H^+]}{K_w} + H_{13} + \frac{10^6}{WRT}} \quad (20)
$$

$$
P_{SO_2} = \frac{\frac{P_{SO_2}^\circ}{RT} \frac{10^6}{W}}{\frac{K_7 K_6 H_5}{[H^+]\gamma^2+\gamma^{2-}} + \frac{K_6 H_5}{[H^+]\gamma^+\gamma^-} + H_5 + \frac{10^6}{WRT}} \quad (21)
$$

$$
P_{CO_2} = \frac{\frac{P_{CO_2}^\circ}{RT} \frac{10^6}{W}}{\frac{K_4 K_3 H_2}{[H^+]\gamma^2+\gamma^{2-}} + \frac{K_3 H_2}{[H^+]\gamma^+\gamma^-} + H_2 + \frac{10^6}{WRT}} \quad (22)
$$

$$
P_{HNO_3} = \frac{\frac{P_{HNO_3}^\circ}{RT} \frac{10^6}{W}}{\frac{K_{12}H_{11}}{[H^+]\gamma^+\gamma^-} + H_{11} + \frac{10^6}{WRT}} \quad (23)
$$

$$
P_{H_2O_2} = \frac{\frac{P_{H_2O_2}^\circ}{RT} \frac{10^6}{W}}{H_{16} + \frac{10^6}{WRT}} \quad (24)
$$

$$
P_{O_3} = \frac{\frac{P_{O_3}^\circ}{RT} \frac{10^6}{W}}{H_{15} + \frac{10^6}{WRT}} \quad (25)
$$

Here $W$ denotes the liquid water content of cloud (g m$^{-3}$), $R$ is the gas constant (0.0821 M atm$^{-1}$ K$^{-1}$), $T$ is the temperature in Kelvin. Since the system under consideration is in equilibrium, the effective concentration i.e. the activity coefficients for various ions are needed in Eqn. (20)–(25). The activity coefficients $\gamma^+$ and $\gamma^-$ are given by the following equations according to Debye-Hückel theory:

$$
log_{10}\gamma^{z+} = log_{10}\gamma^{z-} = -Az^2 \left[ \frac{\sqrt{I}}{(1+\sqrt{I})} - 0.2I \right],
$$
$$
(z = 1, 2, ..) \quad (26)
$$

with A = 0.509 and the ionic strength I is given by

$$
I = 0.5 \sum_i [i] z_i^2 \quad (27)
$$

In Eqns. (25) and (27), $[i]$ and $z_i$ are the concentration and valency of the $i$ ions, respectively.

Substituting Eqns. (20)–(25) into Eqn. (18) and then using (25), $[H^+]$ may be obtained iteratively [Ohta et al., 1981]. The concentration of various ions can be obtained from the calculated $[H^+]$ concentration. The rate of aqueous phase sulfur oxidation depends upon the concentration of dissolved reactants, while oxidation will in turn modify the concentration of reactants in cloud water [Walcek and Taylor, 1986]. There may be number of mechanisms, which contribute to aqueous phase oxidation of $SO_2$ to $SO_4^{2-}$, this study considers sulfate production only by hydrogen peroxide and ozone. They are chosen because they were identified as important reactions by a previous sensitivity analysis of comprehensive aqueous phase chemical mechanism for cloud chemistry [Pandis and Seinfield, 1989]. The rate expression and rate constants for [S(IV)] with $H_2O_2$ and $O_3$ reactions are taken from Hoffmann and Calvert [1985]. We have,

$$
-\frac{d[S(IV)]}{dt} = J_i[S(IV)][A] \quad (28)
$$

here $[A]$ symbolizes the concentration of co-reactant, $[S(IV)]$ identifies a particular $[S(IV)]$ species. The concentration of sulfur species and $[H^+]$ used in the foregoing oxidation process are calculated using the equilibrium model as described above. Their associated rates $J_i$ (M$^{-1}$ s$^{-1}$) are listed in Table 3. Conversion of $[S(IV)]$ to $[S(VI)]$ is updated in time, with chemical equilibrium being reestablished at the end of each incremental oxidation step, using

$$
[S(VI)]_{t+\Delta t} = [S(VI)]_t + \frac{d[S(VI)]}{dt}\Delta t \quad (29)
$$

$$
[S(IV)]_{t+\Delta t} = [S(IV)]_t - \frac{d[S(VI)]}{dt}\Delta t \quad (30)
$$

The aqueous phase reaction is proceeds on a much smaller timescale (2 min) than the model time-step of 30 min [Boucher et al., 2002; Snider and Vali, 1994; Hegg and Hobbs, 1981].

## 2.3. Aerosol module

The present aerosol module is adapted from the Regional Particulate Model [Binkowski and Shankar, 1995], is also a part of Model-3 of U.S. Environment Protection Agency (EPA). The vapor sulfuric acid produced in the gas phase is utilized as an input to the aerosol module which calculates aerosol mass and number density. The aerosol size distribution is represented by a bi-modal log-normal distribution (Eqn. 31). The two modes correspond to the particles with diameter less than 2.5 $\mu$m (PM2.5) and are called the nucleation (Aitken) and accumulation modes. The Aitken mode includes particles up to 0.1 $\mu$m diameter while the accumulation mode covers the range from 0.1 to 2.5 $\mu$m. Thus, we have

$$
n(\ln D) = \frac{N}{\sqrt{2\pi}\ln\sigma_g} \exp\left[-0.5\left(\frac{\ln\frac{D}{D_g}}{\ln\sigma_g}\right)^2\right] \quad (31)
$$

where $D$ is the particle diameter, $D_g$ and $\sigma_g$ are the geometric mean diameter and geometric standard deviation, respectively. The values of $\sigma_g$ are fixed at 1.6 (Aitken mode) and 2.0 (accumulation mode). Conceptually within the fine group, the smaller Aitken mode ($i$) represents fresh particles from nucleation, while the larger accumulation mode ($j$) represents aged particles. The two modes interact with each other through coagulation. Each mode grows through condensation of gaseous precursors and is subjected to dry and wet depositions. Finally the smaller mode may grow into larger mode and partially merge with it. Five prognostic variables are solved in the model: the $H_2SO_4$ vapor concentration (V); Aitken aerosol mass ($M_i$) and number ($N_i$), accumulation mass ($M_j$) and number ($N_j$) concentrations. The conservation equations for these five variables are

$$
\frac{dM_i}{dt} = Jm_p + R_{ci} - K_{ij}N_iN_jm_{pi} - K_dM_i \quad (32)
$$

$$\frac{dN_i}{dt} = J - \frac{1}{2}K_{ii}N_i^2 - K_{ij}N_iN_j - K_dN_i \qquad (33)$$

$$\frac{dM_j}{dt} = R_{cj} + K_{ij}N_iN_jm_{pi} - K_dM_j \qquad (34)$$

$$\frac{dN_j}{dt} = -\frac{1}{2}K_{jj}N_j^2 - K_dN_j \qquad (35)$$

$$\frac{dV}{dt} = R_g - R_{ci} - R_{cj} - Jm_p \qquad (36)$$

where J is the rate of formation of new particles ($\mathrm{cm^{-3}\ s^{-1}}$), $m_p$ is the moles of sulfate added by each nucleated particle, $R_{ci}$ is the condensation rate ($\mathrm{mol\ cm^{-3}\ s^{-1}}$) onto mode i; $m_{pi}$ is the average moles per particle in mode i, as determined from $M_i$ and $N_i$; $K_d$ is the deposition rate constant ($\mathrm{s^{-1}}$); $R_g$ is the chemical source rate ($\mathrm{mol\ cm^{-3}\ s^{-1}}$) and $K_{ij}$ is the Fuch's form of the Brownian coagulation coefficients ($\mathrm{cm^3\ s^{-1}}$) for collisions between the $i^{th}$ and the $j^{th}$ modes.

The solution of differential equations (32)–(36) can be written as

$$M_i(t + \Delta t) = M_i(t) + \Delta M_i^N + \Delta M_i^G$$
$$+\Delta M_i^C + \Delta M_i^D + \Delta M_i^M \qquad (37)$$

$$N_i(t + \Delta t) = N_i(t) + \Delta N_i^N + \Delta N_i^C$$
$$+\Delta N_i^D + \Delta N_i^M \qquad (38)$$

$\Delta M_i$ and $\Delta N_i$ refer to change in mass and number, respectively for mode $i$ due to nucleation ($N$), growth ($G$), coagulation ($C$), deposition ($D$), and merging ($M$). Likewise the expressions for mode $j$ and $V$, can also be written.

### 2.3.1. Nucleation

It refers to growth due to the addition of new sulfate mass, as well as the formation of new particles [Harrington and Kreidenweis, 1998a, 1998b; Kulmala et al. 1998] from gas phase reactions. Both methods predict the rate of increase in number concentration of particles, J (number per unit volume per unit time) by the nucleation from sulfuric acid vapor. The nucleation rate of new sulfuric acid particles is sensitive to function of acid vapor concentration, relative humidity (RH), and temperature (T). The model considers binary nucleation $H_2SO_4$-$H_2O$ system (Jaecker-Voirol and Mirabel, 1989). In each time step (30 mins), the gas-phase $H_2SO_4$ condenses onto existing aerosol. The nucleation occurs at end of time step, if remaining $H_2SO_4$ concentration exceeds critical concentration ($J_{crit}$),

$J_{crit} = 0.16 \exp(0.1\ T - 3.5\ RH - 27.7)$

These nucleated particles are introduced to the smallest size bin in the model. It is assumed that the new particles are 3.5 nm in diameter [Binkowski and Roselle, 2003]. Using either of these methods, the production rate of new particle mass [$\mathrm{\mu g\ cm^{-3}\ s^{-1}}$] is given by

$$\frac{dM}{dt} = \frac{\pi}{6}\rho\,d_{3.5}^3\,J \qquad (39)$$

and that for number ($\mathrm{cm^{-3}\ s^{-1}}$) is

$$\frac{dN}{dt} = J \qquad (40)$$

where $d_{3.5}$ is the diameter of 3.5 nm particle and $\rho$ is the density of particle (sulfuric acid) at ambient relative humidity [Nair and Vohra, 1975].

### 2.3.2. Growth

Aerosol growth by condensation occurs in two steps, viz., the production of condensable material by chemical reaction, and the condensation and evaporation of ambient volatile species on aerosol particles. The growth rates, $G_{ki}$ and $G_{kj}$, for the $k^{th}$ moment of the $i$ and $j$ modes to vapor condensation is given by:

$$G_{ki} = \frac{dM}{dt}\,\omega_i\left(\frac{k}{3}\right)\frac{\widehat{I}_{ki}}{\widehat{I}_{3i}} \qquad (41)$$

$$G_{kj} = \frac{dM}{dt}\,\omega_j\left(\frac{k}{3}\right)\frac{\widehat{I}_{kj}}{\widehat{I}_{3j}} \qquad (42)$$

The fraction of material injected into each mode are given by coefficients $\omega_i$ and $\omega_j$. $\widehat{I}_{ki}$, $\widehat{I}_{kj}$ are the integrals which contribute to mean condensational growth rate [Binkowski and Shankar, 1995]. The rate of increase of $M$ by vapor condensation is given by

$$\frac{dM}{dt} = \left(\frac{6}{\pi}\right)\left(\frac{1}{\rho}\frac{dC}{dt}\right) \qquad (43)$$

$\frac{dC}{dt}$ is the chemical production rate for the $i$ and $j$ modes.

### 2.3.3. Coagulation

Coagulation is an important mechanism for the growth of freshly nucleated particles and is essential for determining the number concentration of newly formed particles. Coagulation rate for the Aitken and accumulation mode is calculated using Gauss-Hermite numerical quadrature [Giorgi and Chameides, 1986] for all of the coagulation terms. The Brownian coagulation of particles within each mode (intramodal) and between the modes (intermodal) are represented as harmonic means of the coagulation coefficients in the free-molecular ($fm$) and near-continuum ($nc$) particle size ranges. The two intermodal terms $C_{ij}$ and $C_{ji}$ for coagulation between particles from modes $i$ and $j$ are given as

$$C_{ij} = \frac{\widehat{C}_{ij}^{fm}\widehat{C}_{ij}^{nc}}{\widehat{C}_{ij}^{fm} + \widehat{C}_{ij}^{nc}} \qquad (44)$$

$$C_{ji} = \frac{\widehat{C}_{ji}^{fm}\widehat{C}_{ji}^{nc}}{\widehat{C}_{ji}^{fm} + \widehat{C}_{ji}^{nc}} \qquad (45)$$

Intramodal coagulation $C_{ll}$ between particles within mode $l$, where $l$ denotes either mode i or mode j, is given by

$$C_{ll} = \frac{\widehat{C}_{ll}^{fm}\widehat{C}_{ll}^{nc}}{\widehat{C}_{ll}^{fm} + \widehat{C}_{ll}^{nc}} \qquad (46)$$

$\widehat{C}_{ij}^{fm}$ and $\widehat{C}_{ll}^{fm}$ denotes the intermodal and intramodal coagulation rates for the free-molecular size range, respectively.

### 2.3.4. Mode merging

The Aitken mode approaches the accumulation mode by small increments over any model time step when particle growth and nucleation are occurring. Though this phenomenon is quite true in nature, it violates the modeling paradigm that two modes of distinct size ranges must always exist. This phenomenon can be modeled by mode merging as follows. The Aitken mode diameter approaches those of accumulation mode by small increment over any model time step when particle growth and nucleation are occurring. Thus this algorithm transfers number, surface area and mass concentration from the Aitken mode to the accumulation mode when the Aitken mode growth rate exceeds the accumulation mode and the number of particles in the accumulation mode is no larger than that in Aitken mode. The fraction of the total number of Aitken mode particles

greater than $D_{ij}$, the diameter of intersection [Binkowski and Roselle, 2003] between the Aitken and accumulation number distributions, is easily calculated from the complementary error function as

$$F_{num} = 0.5[erfc(x_{num})], \quad x_{num} = \frac{ln(D_{ij}/D_{gi})}{\sqrt{2}\,ln(\sigma_g)} \quad (47)$$

$D_{gi}$ is the geometric mean diameter for the Aitken mode number distribution. This method of particle renaming is analogous to the procedure discussed in Jacobson [1997], where particles are reassigned in the moving center concept of a bin model.

The model treats both number and mass for each mode separately as prognostic variables. i.e. aerosol mass and number in Aitken mode, aerosol mass and number in accumulation mode. The aerosol module is fully described in in Binkowski and Shankar, 1995 and Binkowski and Roselle, 2003.

## 2.4. Deposition schemes

Dry deposition is parameterized through deposition velocities, which are prescribed for each chemical species and surface types. The model uses a simple parametrization, which assumes that the rate of deposition at the surface is directly proportional to the mixing ratio (i.e., concentration) of the respective species in the lowest model layer. The wet removal scheme considers both in-cloud and below-cloud scavenging. Since rainfall is computed at every time step in the GCM, removal of gases and aerosols by rain is parameterized using the model generated precipitation formation rate following Giorgi and Chameides [1986]. For aerosols in-cloud fraction is prescribed. Below-cloud scavenging is considered for aerosols only. The dry and wet deposition scheme are treated as size-dependent (Table 4 and 5). The full description of the aerosol deposition in the LMD GCM is detailed in Verma et al. [2005], Boucher et al. [2002], and Reddy et al. [2005a].

The mass fluxes, simulated by the Tiedtke [1989] scheme, are used to parameterize convective transport of gases and aerosols. Convective transport is performed after wet scavenging in order to avoid upward transport of material that is scavenged by precipitation. Convective transport is applied in a bulk manner without distinguishing between the interstitial and the dissolved fraction of trace gases and aerosols (Table 5).

## 3. Model Results and Discussion

The model has been run in climatological mode for the period of 24 months. The results described in this section are taken from the last 12 months of simulations unless otherwise stated, allowing 12 months spin up time for the model. In this section we evaluate the model performance for oxidant and sulfur species concentrations.

In this section we focus on model simulated winter and summer surface and zonal distribution of the key trace gases DMS, MSA, $SO_2$, sulfate, $O_3$, $H_2O_2$, OH and number concentrations in Aitken and accumulation modes for sulfate particles. Model results are compared to surface data for a period of atleast one year from some remote oceanic sites (mostly those of the Sea-Air Exchange program (SEAREX)). The model results are also evaluated by comparing them to observations from long-term monitoring sites and various field campaigns.

## 3.1. Oxidant fields
### 3.1.1. The hydroxyl radical (OH)

The hydroxyl radical is an important oxidizing agent for many trace gases. The oxidation efficiency of the troposphere is largely determined by the hydroxyl radical and its distribution. OH mainly reacts with methane and halocarbons in the troposphere and limits the amount of these gases reaching the stratosphere. An important consequence of the presence of OH radical is its role in the formation of sulfate in the atmosphere. The simulated OH distribution (Fig. 1) differs substantially during January and July months. The OH distribution is most abundant in tropics and shows up a very strong spatial and seasonal variability [Spivakovsky et al., 2000; Lawrence et al., 1999; Allam et al., 1981]. The distribution largely follows the availability of sunlight and high source strength of ozone ($R_1$-$R_3$ in Table 2). The distribution of OH would be thus expected to vary along in phase with ozone concentration and the solar radiation. In January, the OH distribution is dominant in Southern Hemisphere (SH) whereas the dominance has shifted to Northern Hemisphere (NH) in July. Concentrations which attain a maximum reaching up to $5x10^6$ molec cm$^{-3}$ are simulated during both seasons. Methane also plays an important role in the production of HOx ($R_4$-$R_9$), which is distinctly noticeable in the surface concentrations (Fig. 2) at around $30$–$90°$N where sources of anthropogenic emission lead to elevated levels of OH production. The global annual mean OH concentration simulated by the model is $1.4 \times 10^6$ molec cm$^{-3}$. The lifetime of methane by oxidation of OH calculated in the model is 6.8 years. The estimated global mean OH average concentration and life time of methane are in the range of studies of Wang et al.[1998] and Spivakovsky et al. [2000].

The zonal mean distribution of OH for the months of January and July simulated by the model are depicted in Fig. 2. Like surface concentrations the zonal distribution strongly follows the hemispheric contrast with a dominance over SH in January and over NH in July. Specifically, the peak value of OH fraction in the middle and upper troposphere in the SH are simulated at around $30$–$60°$S in the month of January [Müller and Brasseur 1995; Mickley et al. 1999]. The OH levels in July are more than twice as high over the continents which is attributed to its enhanced production during summer in the NH.

### 3.1.2. Hydrogen peroxide

$H_2O_2$ is generated in the gas phase ($R_{10}$, Table 2) with $HO_2$ molecules, is an important reactant in aqueous phase for the formation of sulfate in cloud by its reaction with $SO_2$. The surface and zonal distributions of $H_2O_2$ are illustrated in Figs. 3 and 4, respectively. The maximum mixing ratios for $H_2O_2$ are confined mostly in equatorial regions, during January and July months. In addition, the spread is more pronounced in July and extends to the East in the tropical regions. The source of this spread is both transport of $H_2O_2$ from the nearby areas and also local production by gas phase reactions. This prediction turns out to be consistent with the previous three-dimensional model studies of Lawrence et al. [1999]; Boucher et al. [2002]. The zonal mean distribution shows a maximum concentration near the tropics and decreases rapidly with height and towards the poles. The maximum mixing ratios ranging from 750-1500 pptv are centered around $30°$N - $30°$S, which decreases to a factor of three from surface (1500 pptv) to an altitude of 400 hPa isobaric surface (400 pptv). There is a clear contrast in zonal mean $H_2O_2$ in winter and summer months. During the winter SH values are factor of 4 to 5 larger than NH values, while during summer NH values are factor of 4 to 5 larger than NH values.

### 3.1.3. Ozone

The surface mixing ratios of ozone for January and July are shown in Fig. 5. The maximum values up to 50–70 ppbv are estimated in the polluted regions over the NH [Müller and Brasseur 1995; Wang et al. 1998; Mickley et al. 1999; Horowitz et al. 2003; Hauglustaine et al. 2004]. High mixing ratios of ozone are particularly predicted over the East Asia and South Africa (30-40 ppbv) during winter (Fig. 5, left panel) and over Greenland and North America during the summer (Fig. 5, right panel). The $O_3$ mixing ratios increase with the altitude, especially near the tropopause. The simulated ozone concentrations over Russia vary between 5 to 10 ppbv in January and 30 to 50 ppbv in July. The model simulated ozone profile in summer agrees with that of Mickley et al. [1999] and Müller and Brasseur [1995] with an overestimation over NE Asia while wintertime surface ozone concentration in SH seems to be over predicted at 0-60°E by the model. The minimum $O_3$ levels are found during January over the tropics and Northern high latitudes. These result from the combination of strong photochemical destruction near the surface (due to high water vapor and UV light levels), strong vertical mixing caused by upwelling (Hadley cell) and moist convection, and the relatively smaller sources in the tropics. In the Northern high altitudes, low $O_3$ levels are due to the lack of significant local NOx sources, causing less photochemical $O_3$ production.

The $O_3$ zonal profiles during January and July show high concentration of ozone at higher attitude which suggests a close relationship between ozone and the middle and upper troposphere [Müller and Brasseur, 1995]. The simulated zonal ozone profile varies from 5–500 ppbv as shown in Figure 6. The simulated vertical concentration of ozone thus increases with height due to the increasing lifetime of ozone aloft (Logan et al. [1999] and Horowitz et al. [2003]). The lowest mixing ratios ( 5-10 ppbv) are found in the NH in January and in the SH in July. The higher concentrations has a spread starting from equatorial regions to NH during July and to SH during January. Mixing ratios of upto 500 ppbv are simulated during summer over high altitudes in 30-60°N regions. The stratospheric air intrusion in the upper atmosphere is clearly seen in the zonal distribution of ozone. Note that model does not distinguish between the tropospheric and stratospheric chemistry. Previous model estimates show that lightning contributes about 25-30% of ozone mostly limited to tropical latitudes [Chandra et al., 2004; Lelieveld and Dentener, 2000]. We have not included NOx emissions from lighting in the present study and ozone may be underestimated at higher altitudes over the tropical latitudes at maximum by 25%. Mickley et al. [1999] also pointed out that unlike most of other greenhouse gases, ozone has a short chemical lifetime, resulting in an inhomogeneous distribution that is difficult to map out with observations.

It is of interest to see the annual average of OH and ozone simulated zonal profiles in Figs. 2 and 6 respectively in the right panel. While the zonal profiles of both ozone and OH follows a strong hemispheric contrast in January and July months, the simulated annual averages for both the species follows a symmetric distribution along equator [Lawrence et al., 1999]. The maxima in OH zonal distribution lie at surface to about 3km height at around 30oN while in ozone the maximum mixing ratio ( 300 ppbv) is simulated at elevated altitude (300-100 hPa) over NH.

### 3.2. Sulfur species
### 3.2.1. Dimethyl sulfide

Simulated surface DMS distributions for January and July are shown in Fig. 7a. The maximum concentrations (750-1000 pptv) are over oceans at mid and high latitudes in summer with minima over continents. The pattern follows emission distributions but higher concentrations also show up under winter conditions due to very slow loss rates. The model simulates high concentrations within 50-70°S in winter and, over the North Pacific and the North Atlantic Oceans in summer. The surface mixing ratios of DMS are compared with observations at remote oceanic sites. Fig. 8 shows DMS mixing ratios at Amsterdam Island and Cape Grim. The model overestimates the April to September observations by a factor of two at both sites. The DMS mixing ratios are overestimated at mid and high altitudes during the winter season. The possible reason for this discrepancy is attributed to the low oxidation of oceanic source in the model.

### 3.2.2. Methanesulphonic acid (MSA)

MSA is produced by the oxidation of DMSO. The surface MSA distribution in January and July months is shown in Fig. 7b. Simulated MSA are about 100–150 pptv during January over marine regions. MSA production shows a shift over the North Atlantic Ocean during July. As shown in Fig. 8, the model captures well the MSA concentrations at Midway. Like DMS, model overestimates the MSA concentrations at Samoa and Cape Grim within a factor of 2 to 3. It may be noted that departures between model and observations arises from the fact that the comparison is done between climatologically driven model results while the observations are representative of specific year made at particular location and time. A reason for this overestimation can possibly be due to poor representation of sources.

### 3.2.3. Sulfur dioxide

The modeled surface concentrations of $SO_2$ for the January and July months are depicted in Fig. 7c. The distribution of $SO_2$, primarily controlled by the anthropogenic emissions. Over the remote oceanic regions, $SO_2$ is largely determined by its production following the oxidation of DMS. Elevated concentrations are estimated over the continents, where intense anthropogenic sources exist. During the winter time a high concentration zone is visible over Europe because of meteorological conditions prevalent. Maximum mixing ratios exceeding 6,000 pptv are simulated over polluted regions in the NH. Concentration over marine areas range between 10 to 150 pptv. A comparison between modeled and measured $SO_2$ surface concentrations at Amsterdam Island is shown in Fig. 8. The seasonal variation in measurements is well captured by the model [Boucher et al.2002; Putaud et al. 1992]. The absolute values of model are about a factor of 2 lower than measurements.

### 3.2.4. Sulfate

The highest sulfate concentrations are predicted over Europe (Fig. 7d). There is significantly more sulfate over the NH than over the SH following from the distribution of sulfate precursor ($SO_2$) and stronger OH distribution over NH. The maxima in the sulfate concentration lie close to its precursors sources in the polluted regions of the NH. Higher mixing ratios exceeding 5000 pptv are simulated over this hemisphere (Northern America, Western Europe, and Southeast Asia) during summer. The most striking features in the calculated sulfate distribution are that high mixing ratios occur in summer in comparison to winter. Sulfate production rates are more pronounced via increased gas-phase production during July over NH, when abundant sunlight is available. Also a plume of sulfate can be seen extending from continents towards oceanic regions originating from major $SO_2$ emitting regions. The sulfate lifetime is about twice that of $SO_2$. Again, Sulfate is formed downwind of $SO_2$, over the oceanic regions. The tropical and northern subtropical sulfate concentrations are higher in NH winter

than summer. The large cloud cover favors efficient aqueous phase reactions producing large amounts of sulfate in these regions. A comparison between the modeled and measured sulfate surface concentrations at remote oceanic sites (Mawson, Midway and Fanning Island) is shown in Fig. 8. The seasonal cycle in the measurements is well captured by the model at Mawson. The measurements at Fanning Island and Midway do not show any seasonality. The modeled sulfate mixing ratio at wintertime are underestimated.

The vertical profile of sulfate shows maximum values in latitude belts of industrial activity (30°N–60°N) with a vertical spread upto 100 hPa into the free troposphere during summer (Fig. 9). The seasonal differences caused, by more rapid summertime formation of OH, affect the tropical regions. During July, the convective activity could perhaps have pumped the sulfate into elevated layers in the model. Specifically, tropical and northern subtropical Sulfate concentrations are much higher over NH winter than summer at all tropospheric levels. In the upper troposphere the predicted concentrations reach values upto 250 pptv, due to inefficient wet scavenging at these altitudes.

### 3.3. Sulfur species at continental/polluted areas

In order to discuss the behavior of the model at different latitudes and longitudes, we compare the modeled and observed surface values at representative sites in Europe and North America.

The model fairly captures the concentration variations of $SO_2$ while it underestimates $SO_2$ in winter as shown in Fig. 10 (upper panels) at Cree Lake, Aspvreten and Krvatn sites, which are all located north to 50°N. This discrepancy might be related to deficiency of sulfur oxidation in wintertime. Modeled $SO_2$ is over predicted at mid-latitude sites during all seasons (middle row, Fig. 10), while the modeled concentrations at 25-35°N agree well with the observed seasonal variations within a factor of two.

Fig. 11 illustrates the seasonal variation of sulfate concentrations at some selected sites. The model overpredicts the sulfate mixing ratios northward to latitude circle 55°N at Aspvertn, Cree Lake and Krvatn. The model estimates are in good agreement with observations when compared southward to 40°N at Whiteface, Caryville and Everglades. At Montelibretti, wintertime sulfate mixing ratios are underestimated due to insufficient wintertime $SO_2$ oxidation. Also the model fails to reproduce the high mixing ratios during springtime at Bells (35.75°N, 89.13°W). As it may be noted, the agreement is good, within a factor of 2-3 over most areas between calculated sulfate concentrations and observations. At Aspvertn, Cree Lake and Krvatn the predicted seasonal cycle is however, not in phase of observed sulfate concentrations.

It is of interest to compare the sum of seasonal cycle of $SO_2$ and sulfate (total S) with measurements (Fig. 12). The agreement between model and observations for total S improves as compared to $SO_2$ and sulfate (Figs. 10 and 11). The discrepancy between model and observations for total S is largely contributed by sulfate rather than $SO_2$.

Over North America and Europe measurements of atmospheric sulfate are available for the last 2 decades. Over North America we compare modeled sulfate at surface with IMPROVE (Interagency Monitoring of Protected Visual Environments) network measurements. Monthly mean concentrations are constructed using available data for the period

1990 to 2000. During winter period model values are underestimated. Modeled values are within a factor of 2 of measurements during the summer period. Comparison between model and measurements improves on annual mean basis. Over Europe we compare modeled surface level sulfate with EMEP measurements. Once again we use available data for the period 1990 to 2000. Over Europe, during the winter the agreement seems to be good between model and measurement. During the summer model tends to overestimate sulfate. The over estimation of sulfate by model is attributed to high $SO_2$ conversion into sulfate due to less wet deposition rate simulated by the model over Europe in summer. Once again the agreement between model and measurements improves on annual mean basis.

### 3.4. Vertical distribution of sulfur species

The model performance for sulfur species in the middle and upper troposphere is assessed here. The observations constitute measurements obtained from the field campaigns in the Pacific Ocean: Pacific Exploratory Mission PEM-West A (September-October 1991), PEM-West B (February-March 1994), and PEM-Tropics-A (August-October, 1996). The model results have been averaged over the selected regions for measurements periods: February-March for the PEM-West B intensive campaign, September-October for the PEM West A, and PEM-Tropics A campaigns. It may be noted that departures from one-to-one agreement between model results and observations arises from the fact that the model values are from climatological run while the observations are for particular location and time.

#### 3.4.1. Dimethyl sulfide
Observed DMS mixing ratios at surface range anywhere between 20 to 200 pptv depending upon the location, and the model is able to reproduce these values. Both observed and modeled DMS concentrations (Fig. 14) decrease very rapidly with altitude. Oceanic sources are most affected by intra-annual variations. Over some regions model values are underestimated at higher altitudes by a factor of 2 to 3.

#### 3.4.2. Sulfur dioxide
The agreement between model results and observations of the vertical distribution of $SO_2$ is variable (Fig. 15). Surface $SO_2$ mixing ratios are overestimated over Japan and Hong Kong areas with a factor of 2-3 but agree well with the observations around Guam. The model fails to reproduce the concentration peaks of $SO_2$ observed in the boundary layer and free troposphere over Japan and Hong Kong sites for PEM-West B. This could be due to non resolution of boundary layer in the global model. Notably, the model results agree with observations for Eastern Pacific (PEM-Tropics A) with observed peaks in $SO_2$ in the boundary layer being reproduced.

#### 3.4.3. Sulfate
The model is able to produce the general trend in vertical distribution of sulfate over nearly all regions (Fig. 16). Like $SO_2$ vertical profile, sulfate mixing ratios are well predicted by the model at Guam and Japan while the mixing ratios are underestimated in boundary layer near Hong Kong and overestimated at surface for Central Pacific and Fiji

#### 3.4.4. Hydrogen peroxide
Although the model overestimates $H_2O_2$ concentration (Fig. 17) in PEM-West B mission at Japan and Guam areas, comparisons of the simulated $H_2O_2$ vertical profile seems to be in broad agreement with the observations during the PEM campaign. The surface and the boundary layer mixing ratios are mostly reproduced.

## 4. Sulfate number concentration

The sulfate number concentrations are predicted in the Aitken and accumulation modes. Aitken mode number concentrations follow the primary sulfur emissions and therefore highest in the lower troposphere close to source regions of anthropogenic emissions. The higher Aitken ($1.4 \times 10^4$ particles cm$^{-3}$) number concentrations (Fig. 18) are visible in the lower tropical troposphere, where the nucleation is favored by the available temperature and R.H. Accumulation mode concentrations are mainly confined in the lower troposphere along the continents. The declining concentrations to remote regions from continents is attributed to the wet and dry deposition/gravitational settling of these large particles. The summer and the winter time size distribution at surface represents the characteristic features that of van Dingenen et al. [2004], where the larger number concentration is observed at urban sites (upto $2 \times 10^4$ particles cm$^{-3}$) during summer. Fig. 19 shows the zonal distribution of Aitken mode and the total accumulation mode sulfate number concentrations for the January and July. In general, there is a declining vertical gradients for both Aitken and accumulation modes number concentration in each hemisphere. However, an elevated Aitken mode concentration in the upper troposphere can be observed during January at about 60°S from 800–600 hPa level (1000 particles cm$^{-3}$); possibly, small particles may have been pumped to higher altitudes by the convective activity and DMS conversion. The zonal number concentrations in July are greater than that of January. However, the concentrations are higher over NH during both of these months over 30-60°N latitudinal band.

We compare the modeled number concentrations profiles with long-term available aerosol number concentration observations at selected regions and adopt the same classification devised by Wilson et al. [2001]. The modeled values over American Samoa are the average concentrations in the lowest 500 m layer, while at Mauna Loa are the average concentrations for the 2.5 to 4.7 km model layer (Fig. 20). The model is not likely to reproduce the variability in the observations at a specific location due to difference in model meteorology. There are meagre compilations of observations available on size distribution properties for sulfate aerosols. Over these selected sites (Fig 20) the observations indicate an internal mixture of aerosol while the modeled aerosol size distribution represents only sulfate particles, an extensive quantitative model evaluation is therefore not yet possible. Nevertheless, for the reason of further evaluation, the PM2.5 mass and accumulation mode particle number concentrations are plotted. The simulated accumulation mode to sulfate surface level grid boxes over the North Atlantic are given in Fig. 21. The modeled ratios lie in the range of $500 \pm 250$ particles cm$^{-3}$, are consistent with the results of Wilson et al. [2001] and van Dingenen et al. [2004]; which represents the minimum particle number concentration associated with a given PM2.5 loading at clean and rural sites. It should be noted that the particle concentrations in Fig. 22 refers to sulfate number concentration in the accumulation mode, while Wilson et al. [2001] gives the number concentration in accumulation mode with combined sea-salt and two mixed mode of BC, OC, and sulfate modes.

Notably, the number concentration at surface and zonal distributions shown in Figs. 18 and 19, respectively are in qualitative agreement with the observations and the previous global model studies [Raes et al. 2000; Wilson et al. 2001; Stier et al. 2004]. The decrease in accumulation mode particles and Aitken mode concentrations as noted in the simulated zonal profiles (Fig. 19) are consistent with the vertical profile measurements by Raes et al. [2000].

## 5. Budget of Sulfur Species

The global annual budget of $H_2O_2$ is summarized in Table 6. The global source of $H_2O_2$ is 1836 mg $H_2O_2$ m$^{-2}$ yr$^{-1}$ which result from the $HO_2 + HO_2$ reaction. The sinks for $H_2O_2$ are photodissociation (32%), the reaction with OH (30%), wet scavenging (22%), and dry deposition (12%). The present estimate of global mean burden (3.0 Tg) and lifetime (1.2 days) are in close agreement with estimates of Koch et al. [1999].

The global DMS emissions of 20.7 Tg S yr$^{-1}$ are in the range of previous estimates by Feichter et al. [1996] and Pham et al. [1995]. Globally and annually simulated sulfur budget in the model is presented in Fig. 22. The model simulates a mean lifetime of 1.2 days with a global burden of 0.07 Tg S for DMS. The global annual $SO_2$ emissions are 91.8 Tg S yr$^{-1}$ less than the estimates by Pham et al. [1995] of 123 Tg Syr$^{-1}$ and Chin et al. [1996] of (96 Tg Syr$^{-1}$). The estimated $SO_2$ lifetime is 1.1 days with global burden of 0.24 Tg S in agreement with Chin et al. [1996] and Boucher et al. [2002]. The dry deposition accounts for 46% of total sink with small compliment from wet deposition of 3% The gas phase oxidation depletes 15% of total $SO_2$ while the in-cloud oxidation accounts for remaining 36% of total sink. The total simulated source of sulfate (47.4 Tg S yr$^{-1}$) consists of $SO_2$ oxidation and a small contribution (5% of $SO_2$ anthropogenic sources) from direct sulfate emissions (3.31 Tg S yr$^{-1}$). The wet scavenging removes about 75% of total sulfate with dry deposition accounting for remaining 25%. The estimated sulfate lifetime is 4.9 days with global burden of 0.63 Tg. The budget and lifetimes of $SO_2$ and sulfate simulated in the present work are shown in Table 7 along with other model studies. The present estimate of burden is in the range of previous studies: 0.6 Tg S of Rasch et al. [2000] and 0.56 Tg S of Boucher et al. 2002. However, the present sulfate burden is lower than the standard case 0.72 Tg S of Koch et al. [2003], 0.8 Tg S of Langer and Rodhe [1991] and 1.1 Tg S of Chin et al. [1996].

The sulfate column burden is important because it leads directly to assessment of enhanced albedo by direct light scattering. The identification of different chemical pathways to the sulfate production is thus important. This helps to understand the importance of different chemical pathways to sulfate production and atmospheric burden. These results help to reduce the uncertainty in the oxidant fields and sulfate estimates. We compute separately gas phase production (GPP) and aqueous phase production (APP) of sulfate. The estimation is done by conducting two simulations: a simulation with both APP and GPP productions and the other simulation in which APP is shut down for sulfate production while still depleting $SO_2$. Most of the sulfate is produced in the aqueous phase (about 71%); it has relatively short lifetime (2.9 days on global average). On the other hand contribution from GPP to sulfate production is only 29% with a lifetime of 11.3 days. In contrast to production, the contribution GPP to the annual mean sulfate burden is 55% with remaining 45% from APP. It is interesting to note that while most of the sulfate is produced in the aqueous phase (31.3 Tg S i.e. 71%), the sulfate burden is much more pronounced by GPP. The APP production takes place within the clouds and favors a efficient wet scavenging of the freshly formed sulfate.

The visualization of sulfate burden and production rates for GPP and APP as a function of month (Fig. 23) provides a clear view on the seasonal cycle of these two pathways. While GPP contributes more efficiently to the sulfate burden (Fig. 23a) than does aqueous-phase conversion, the

variation in monthly sulfate production rate (Fig. 23b) suggests that the APP production rate dominates throughout the year. This explains the large contribution to sulfate production but rather small contribution to atmospheric burden. The sulfate burden (Fig. 23a) shows distinct seasonality with a more than 40% sulfate burden in July than in January. The maximum GPP burden is estimated in April-October period while in APP the maximum burden is estimated during January-March period. Our results indicate that GPP and APP sulfate production rates exhibit inverse relationship. The GPP production rate is maximum in July (Fig. 23b) while it is minimum in the month of July for APP. During the summer period higher insolation and subsequent enhanced photolysis rate and increase in OH levels result in higher sulfate formation through GPP. The APP production varies in phase to the in-cloud oxidation of $H_2O_2$ and $O_3$ during January-March Period.

Figs. 24 and 25 show the surface sulfate concentration by GPP and APP, respectively for January and July. As depicted by the monthly evolution time series of sulfate burden, GPP is highest in the July month over the tropics, Europe and part of North America with values ranging from 1500-3000 pptv during this period. There is some tendency for aqueous phase production to be higher at continents (near source regions) since this pathway is faster than gas-phase oxidation. Unlike GPP, the APP is pronounced in the month of January over Europe (600-1400 pptv).

## 6. Conclusions

In this study, we provide a first description of a newly developed interactive sulfur chemistry (gas and aqueous-phase) with a comprehensive aerosol module and its implementation in the Laboratoire de Météorologie Dynamique General Circulation Model. The model predicts the transport, distribution and photochemical formation rates of tropospheric sulfate mass and number concentration and mixing ratios of the gases like $O_3$, $H_2O_2$, CO, NOx with several short lived radicals like OH and $OH_2$. The sulfate mass and number concentrations in the Aitken and accumulation modes are predicted considering size-segregated aerosol dynamics.

The model performance is thoroughly validated by comparing predicted oxidants and sulfur species concentrations with measurements at different parts of the World. The model simulated chemical constituents are in agreement within a factor of 2 to 3 of measurements.

Modeled surface concentration fields show encouraging agreement in spatial patterns and temporal episodicity with comparable magnitudes of observed quantities. Our global DMS source of 20.7 Tg S $yr^{-1}$ affords a good simulation of sulfate concentrations at remote oceanic sites.

Aqueous phase pathway accounts for most of the sulfate production (about 71%) with a relatively short lifetime of 2.9 days. The contribution of gas-phase pathway to sulfate production is at 29% with longer lifetime of 11.3 days. The longer lifetime of sulfate produced by gas-phase pathway results in contribution of 55% to the total atmospheric burden. The short lifetime for aqueous phase can be explained by the fact that, it takes place within the clouds and favors a efficient wet scavenging of freshly formed sulfate.

In conclusion, the three dimensional interactive chemical transport model for tropospheric sulfate described here appears to be a useful tool for examining sulfate concentrations and burden on sub-hemispheric to global scales. The model employs the appropriate description of formation and removal processes for sulfate aerosols and includes a size segregated dynamics. The model evaluation gives values for turnover times and yields, that are consistent with the previous global model studies. The size segregated aerosol mass and number concentration will be extended to calculate the sulfate direct and indirect radiative forcing.

## References

Ackermann, I. J., Hass, H., Memmesheimer, M., Ebel, A., Binkowski, F. S., and Shankar, U., Modal aerosol dynamics for Europe: Development and first applications, Atmos. Environ., 32 (17), 2981-2999, 1998.

Adams, P.J., J.H. Seinfeld, D. Koch, L. Mickley, and D.J. Jacob, General circulation model assessment of direct radiative forcing by the sulfate-nitrate-ammonium inorganic aerosol system, J. Geophys. Res., 106, 1999.

Adams, P.J., and J.H. Seinfeld, Predicting global aerosol size distributions in general circulation models, J. Geophys. Res., 107, 2002.

Allam, R., J., Groves, K., S., and Tuck, A., F., Global OH distribution derived from general circulation model fields of ozone and water vapor, J. Geophys. Res., 86, 5303-5320, 1981.

Atkinson, R., Baulch, D. L., Cox, R. A., Hampson, R. F., Kerre Jr., and Troe, J. A., Evaluated kinetic and photochemical data for atmospheric chemistry: Supplement III, J. Physical and Chemical Ref. Data 18, 881-1097, 1989.

Berge, E., Coupling of wet scavenging of sulphur to clouds in a numerical weather prediction model, Tellus, 45 B, 1-22, 1993.

Binkowski, F. S., and Shankar, U., The regional particulate matter model: Part 1, model description and preliminary results, J. Geophys. Res., 100, 26,191-26,209, 1995.

Binkowski, F. S., and Roselle., S. J., Models-3 community multiscale air quality (CMAQ) model aerosol component 1. model description, J. Geophys. Res., 108 (D6), 4183, doi:10.1029/2001JD001409, 2003.

Boucher, O., and Lohmann, U., The sulfate-CCN-cloud albedo effect: a sensitivity study using two general circulation models, Tellus 47B, 281-300, 1995.

Boucher, O., Pham, M., and Venkataraman, C., Simulation of the atmospheric sulphur cycle in the Laboratoire de Météorologie Dynamique general circulation model: Model description, model evaluation, and global and European budgets, Note scientifique de l'IPSL n° 23, 32pp, 2002.

Charlson, R. J., Schwartz, S. E., Hales J. M., Cess, R. D., Coakley, J. A., Hansen, J. E., and Hotmann, D. J., Climate forcing by anthropogenic aerosols, Science 255, 423–430, 1992.

Chatfield, R. B., and Crutzen, P. J., Are there interactions of iodine and sulfur species in marine air photochemistry? J. Geophys. Res., 95, 22319-22341, 1990.

Chang, J. S., Brost, R. A., Isaksen, I. S. A., Madronich, S., Middleton, P., Stockwell, W. R., and Walcek, C. J., A three dimensional Eulerian acid deposition model: Physical concepts and formulation, J. Geophys. Res., 92, 14681-14700, 1987.

Chen, J-P., and Crutzen, P. J., Solute effect on the evaporation of ice particles, J. Geophys. Res., 99, 18, 847-18, 859, 1994.

Chin, M., Jacob, D., Gardner, G.M., Foreman-Fowler, M.S., and Spiro, P.A., A global three dimensional model of tropospheric sulphate, J. Geophys. Res., 101, 18, 667-18, 690, 1996.

Crutzen, P. J., and Lawrence, M. G., The impact of precipitation scavenging on the transport of trace gases, J. Atmos. Chem., 37, 81-112, 2000.

Feichter, J., Kjellstrom, E., Rodhe, H., Dentener, F., Lelieveld, J., and Roelofs, G.-J., Simulation of the tropospheric sulphur cycle in a global climate model, Atmos. Environ., 30, 1693-1707, 1996.

Giorgi, F., and Chameides, W. L., Rainout lifetimes of highly soluble aerosols and gases as inferred from simulations with a general circulation model, J. Geophys. Res., 91, 14,367-14,376, 1986.

Harrington, D. Y. and Kreidenweis, S. M., Simulations of sulfate aerosol dynamics: Part I model description, Atmos. Environ., 32, 1691-1700, 1998a.

Harrington, D. Y. and Kreidenweis, S. M., Simulations of sulfate aerosol dynamics: Part II model intercomparison, Atmos. Environ., 1701-1709, 1998b.

Hauglustaine, D. A., Hourdin, F., Jourdain, L., Filiberti, M.-A., Walters, S., Lamarque, J.-F., and Holland, E. A., Interactive chemistry in the Laboratoire de Météorologie Dynamique general circulation model: description and background tropospheric chemistry evaluation, J. Geophys. Res., 109, D04314, doi:10.1029/2003JD003957, 2004.

Hegg, D. A., and Hobbs, P. V., Cloud water chemistry and the production of sulfates in clouds, Atmos. Environ., 15, 1597-1604, 1981.

Hesstvedt, E., Hov, Ö., and Isaksen, I. S. A., Quasi-steady-state-approximation in air pollution modelling: comparison of two numerical schemes for oxidant prediction, Int. J. Chem. Kinet., 10, 971–994, 1978.

Hoffmann, M.R., and Calvert, J.G., Chemical transformation modules for Eulerian acid deposition models, volume 2, The aqueous phase chemistry EPA/600/3-85/017, US Environmental Protection Agency, Research Triangle Park, North Carolina, USA.

Horowitz, L.W., et al., A global simulation of tropospheric ozone and related traces: Description and evaluation of MOZART, version 2, J. Geophys. Res., 108(D24), 4784, doi:10.1029/2002JD002853, 2003.

Hourdin, F., and Armengaud, A., On the use of finite volume methods for atmospheric advection of trace species: I. Test of various formulations in a general circulation model, Mon. Wea. Rev., 127, 822-837, 1999.

Jaecker-Voirol, and Mirabel, A. P., Heteromolecular nucleation in the sulfuric acid-water system, Atmos. Environ., 23, 2053-2057, 1989.

Jacobson, M.Z., Development and application of new air pollution modelling system, II, Aerosol module structure and design, Atmos. Environ., 31, 131-144, 1997.

Jones, A., Roberts, D. L., Woodage, M. J., and Johnson, C. E., Indirect sulphate aerosol forcing in a climate model with an interactive sulphur cycle, J. Geophys. Res., 106, 20,293-20,310, 2001.

Kettle, A. J., et al., A global database of sea surface dimethylsulphide (DMS) measurements and a procedure to predict sea surface DMS as a function of latitude, longitude and month. Global Biogeochemical Cycles 13, 399-444, 1999.

Kiehl, J. T., and Briegleb, B. P., The relative role of sulphate aerosols and greenhouse gases in climate forcing, Science, 260, 311-314, 1993.

Knut, R., Isaksen, I.S.A., and Berntsen, T. K., Global distribution of sulphate in the troposphere: A three-dimensional model study, Atmos. Environ., 32(20), 3593-3609, 1998.

Koch, D., Park, J., and del Genio A., Clouds and sulphate are anticorrelated: A new diagnostic for global sulphur models, J. Geophys. Res., 108(D24), 4781, doi:10.1029/2003JD003621, 2003.

Kulmala, M., Laaksonen, A., and Pirjola, L., Parameterization for sulphuric acid/water nucleation rates, J. Geophys. Res., 103, 8301-8307,1998.

Langer, J., and Rodhe, H., A global three dimensional model of tropospheric sulphur cycle, J. Atmos. Chem., 13,225–263, 1991.

Lawrence, M. G., Crutzen, P. J., Rasch, P. J., Eaton, B. E., and Mahowald, M., A model for studies of tropospheric chemistry: Description, global distributions, and evaluation, J. Geophys. Res., 104, 26,245-26,277, 1999.

Liao, H., et al., Interactions between tropospheric chemistry and aerosols in a unified general circulation model, J. Geophys. Res., 108, 2003.

Liss, P.S., Merlivat, L., Air-sea exchange rates: Introduction and synthesis, in the role of Air-Sea Exchange in geochemical cycling, P. Buat- Menard (Ed.), Norwell, Mass, 1986.

Ohta, S., Okita, T., and Kato, C., A numerical model of acidification of cloud water, J. Meteor. Soc. Japan, 6, 59, 1981.

Mickley, , J. Geophys. Res., , 1999.

Müller, J.-F., and G.P. Brasseur, IMAGES: A three-dimensional chemical transport model of the global troposphere, J. Geophys. Res., 100, 16,445-16,490, 1995.

Pandis, S.N., and J.H. Seinfeld, Sensitivty analysis of a chemical mechanism for aqueous phase atmospheric chemistry, J. Geophys. Res., 94, 1105-1126, 1989.

Pham, M., Müller, J.-F., Brasseur, G., Granier, C., and Mégie, G., A 3-D model study of the global sulphur cycle: Contributions of anthropogenic and biogenic sources, Atmos. Environ., 30, 1815-1822, 1995.

Pruppacher, H. R., and Klett, J. D., Microphysics of Clouds and Precipitation, second revised and enlarged edition with an introduction to cloud chemistry and cloud electricity, Kluwer Academic Publishers, Boston, 954 pp., 1997.

Putaud, J.-P., Mihalopoulos, N., Nguyen, B.C., Campin, J.M., Belviso, S., Seasonal variations of atmospheric sulphur dioxide and dimethylsulphide concentrations at Amsterdam Island in the Southern Indian Ocean. J. Atmos. Chem., 15, 117-131, 1992.

Raes, F., Dingenen, R. V., Vignati, E., Wilson, J., Putaud, J-P., Seinfeld J. H., and Adams, P., Formation and cycling of aerosols in the global troposphere, Atmos. Environ., 34, 4215-4240, 2000.

Rasch, P.J., Barth, M. C., Kiehl, J. T., Schwartz, S.E., and Benkowitz, C.M., A description of the global sulphur cycle and its cotrolling processes in the National Centre for Atmospheric Research Community Climate Model, Version 3, J. Geophys. Res., 105(D1), 1367-1385, 2000.

Reddy, M. S., and O.Boucher, A study of the global cycle of carbonaceous aerosols in the LMDZT general circulation model, J. of Geophys. Res., 109(D14), D14202, doi:10.1029/2003JD004048, 2004.

Reddy, M. S., O. Boucher, N. Bellouin, M. Schulz, Y. Balkanski, J. Dufresne, and M. Pham (2005), Estimates of global multicomponent aerosol optical depth and direct radiative perturbation in the Laboratoire de Météorologie Dynamique general circulation model, J. Geophys. Res., 110, D10S16, doi:10.1029/2004JD004757.

Reddy M. S., O. Boucher, Y. Balkanski, M. Schulz (2005), Aerosol optical depths and direct radiative perturbations by species and source type, Geophys. Res. Lett., 32, L12803, doi:10.1029/2004GL021743.

Sadourny, R., and Laval, K., January and July performances of LMD general circulation model. New perspectives in Climate Modelling, A. Berger, Ed., Elsevier, pp. 173-198, 1984.

Schwartz, S.E., Mass-transport considerations pertinent to aqueous-phase reactions of gases in liquid-water clouds, Chemistry of Multiphase Atmospheric Systems, edited by W. Jaeschke, pp. 415-471, Springer, NewYork, 1986.

Snider, J. R. and Vali, G., Sulphur dioxide oxidation in winter orographic clouds, J. Geophys. Res., 99, 18713-18733, 1994.

Spivakovsky, C., M., Logan, J., A., et al., Three dimentional climatological distribution of tropospheric OH: update and evaluation, J. Geophys. Res., 105, 8931-8980, 2000.

Stier, P., Feichter, J., Kinne, S., Kloster, S., Vignati, E., Wilson, J., Ganzeveld, L., Tagen, I., Werner, M., Balkanski, Y., Schultz, M., and Boucher, O., The aerosol-climate model ECHAM5-HAM, Atmos. Chem. Phys. Discuss., 4, 5551-5623, 2004.

Tiedtke, M., A comprehensive mass flux scheme for cumulus parameterization in large scale models, Quart. J. Roy. Meteor. Soc., 117, 1779-1800, 1989.

Twomey S.A., Pollution and the planetary albedo, Atmos. Environ. 8, 1251-1256 1974.

van Dingenen, R., Raes, F., Putaud., J.-P., et al., A European aerosol phenomenology–I: physical characterstics of particulate matter at kerbside, urban, rural and background sites in Europe, Atmos. Environ., 38, 2561-277, 2004.

van Leer B, Towards the ultimate conservative difference scheme: IV: A new approach to numerical convection. J. Computational Phys., 23, 276-299 1977.

Verma, S., Boucher, O., Reddy, M. S., Deb, S.K., Upadhyaya, H.C., Le Van, P., Binkowski, F. S., and Sharma, O. P., Tropospheric distribution of sulphate aerosol mass and number concentration during INDOEX-IFP and its transport over the Indian Ocean: A GCM study, Atmos. Chem. and Phys. Discussions, 5, 395-436, 2005.

Wang, Y., Logan, J. A., Jacob, D. J., and Spivakovsky, C. M., Global simulation of tropospheric $O_3$-$NO_x$-hydrocarbon chemistry: 2. Model evaluation and global ozone budget, J. Geophys. Res., 103, 10,727-10,755, 1998.

Walcek, C. J., and Taylor, R., A theoretical method for computing vertical distribution of acidity and sulfate production with cumulus clouds, J. Atmos. Sci., 43, 339-355, 1986.

Wilson, J., Curvelier, C., and Raes, F., A modeling study of global mixed aerosol fields, J. Geophys. Res., 106, 34081-34108, 2001.

Om Prakash Shamra, Sunita Verma, H.C. Upadhyaya, Centre for Atmospheric Sciences, Indian Institute of Technology, Delhi, INDIA-110016 (verma.sunita@gmail.com); (opsharma@cas.iitd.ac.in); (hcdhyaya@cas.iitd.ac.in), M. Shekar Reddy, NOAA-Geophysical Fluid Dynamics Laboratory, 201 Forestal Road, Princeton, NJ 08542, USA (shekar.reddy@noaa.gov)